Magn Reson Med Sci 2020; 19; 216–226
doi:10.2463/mrms.mp.2019-0061
Published Online: October 15, 2019

MAJOR PAPER

Impact of *b*-Value Sampling Scheme on Brain IVIM Parameter Estimation in Healthy Subjects

Stéren Chabert[1,2,3*], Jorge Verdu[2,4], Gamaliel Huerta[2], Cristian Montalba[5], Pablo Cox[6], Rodrigo Riveros[6,7], Sergio Uribe[3,5,8], Rodrigo Salas[1,2], and Alejandro Veloz[1,2]

Purpose: Intravoxel incoherent motion (IVIM) analysis has attracted the interest of the clinical community due to its close relationship with microperfusion. Nevertheless, there is no clear reference protocol for its implementation; one of the questions being which *b*-value distribution to use. This study aimed to stress the importance of the sampling scheme and to show that an optimized *b*-value distribution decreases the variance associated with IVIM parameters in the brain with respect to a regular distribution in healthy volunteers.

Methods: Ten volunteers were included in this study; images were acquired on a 1.5T MR scanner. Two distributions of 16 *b*-values were used: one considered 'regular' due to its close association with that used in other studies, and the other considered 'optimized' according to previous studies. IVIM parameters were adjusted according to the bi-exponential model, using two-step method. Analysis was undertaken in ROI defined using in the Automated Anatomical Labeling atlas, and parameters distributions were compared in a total of 832 ROI.

Results: Maps with fewer speckles were obtained with the 'optimized' distribution. Coefficients of variation did not change significantly for the estimation of the diffusion coefficient *D* but decreased by approximately 39% for the pseudo-diffusion coefficient estimation and by 21% for the perfusion fraction. Distributions of adjusted parameters were found significantly different in 50% of the cases for the perfusion fraction, in 80% of the cases for the pseudo-diffusion coefficient and 17% of the cases for the diffusion coefficient. Observations across brain areas show that the range of average values for IVIM parameters is smaller in the 'optimized' case.

Conclusion: Using an optimized distribution, data are sampled in a way that the IVIM signal decay is better described and less variance is obtained in the fitted parameters. The increased precision gained could help to detect small variations in IVIM parameters.

Keywords: *brain, diffusion magnetic resonance imaging, intravoxel incoherent motion, neuroimaging*

Introduction

Diffusion MRI is a widely-available technique that provides insight into tissue microstructure. One observation that has drawn growing interest is the differential behavior of the diffusion signal at low *b*-values, which is denominated intravoxel incoherent motion (IVIM).[1–6] At low *b*-values, the signal decays faster. This decay is described through the pseudo-diffusion coefficient (D^*) in area per unit time, through the associated signal fraction (f also called volume fraction of incoherently flowing blood in tissues) and through the diffusion coefficient (D) according to Eq. [1], where S is the signal magnitude of the diffusion-weighted image (DWI) and S_0 is the signal magnitude without diffusion weighting.

[1]CINGS Centro de Investigación y Desarrollo de Ingeniería para la Salud, Universidad de Valparaíso, Valparaíso, Chile
[2]Escuela de Ingenieria Civil Biomedica, Universidad de Valparaíso, General Cruz 222, Valparaíso, Chile
[3]Millennium Nucleus for Cardiovascular Magnetic Resonance, Santiago, Chile
[4]Universidad Politécnica de Valencia, Valencia, España
[5]Center for Biomedical Imaging, Pontificia Universidad Católica de Chile, Santiago, Chile
[6]Servicio de Imagenología, Hospital Carlos van Buren, Valparaíso, Chile
[7]Facultad de Medicina, Universidad de Valparaíso, Valparaíso, Chile
[8]Radiology Department, Pontificia Universidad Católica de Chile, Santiago, Chile
*Corresponding author, Phone: +56-32-2603-653,
Email: steren.chabert@uv.cl

Received: April 25, 2019 | Accepted: August 6, 2019

$$S = S_0\left[fe^{-bD^*} + (1-f)e^{-bD} \right] \quad [1]$$

Although the information obtained through IVIM does not directly correspond to perfusion *per se*, different studies have related IVIM parameters to micro-perfusion and the microvasculature.[7–9] Among all of the different parameters associated with IVIM, the so-called perfusion fraction (*f*) was related to the estimation of dynamic susceptibility contrast-derived cerebral blood volume in the grey matter (GM),[10] to arterial spin labeling (ASL),[11] to capillary volume[12] and to cerebral blood flow.[13]

A somewhat broad range of healthy brain IVIM values (*f* and D^*) are published in the literature and are summarized in Table 1; reported *D* values are more stable across studies. This range of values makes it difficult to determine which healthy reference value to expect. One question that remains unanswered is how to obtain the IVIM parameters reliably from both an acquisition and a processing point of view.

From an acquisition point of view, one of the first questions to be answered when obtaining IVIM values in a patient relates to the number of *b*-values and the choice of distribution of these *b*-values. Sampling strategies for *b*-values were shown to be relevant in studies based on simulations[14,15] or performed in different organs; for example, in breast,[16] liver,[17] kidney[14,15] and prostate.[18] Although some studies concluded that clinically-relevant information could be attained with a low number of *b*-values,[19,20] others showed that the relative error decreased by 40% when the number of *b*-values increased from 4 to 16.[21] Meeus et al.[20] proposed a fast acquisition scheme with a low number of *b*-values[4] and reported that *f* and *D* were of most interest as opposed to D^*, which showed high variability. Similarly, Cohen et al.[22] showed that

Table 1 IVIM values in the brains of healthy volunteers. Data from contralateral hemisphere in studies undertaken in patients were not included here

	f (%)	D^* (× 10^{-3} mm²/s)	*D* (× 10^{-3} mm²/s)
Gray matter			
Average over published values*	10.0 ± 7.4 (2.4–24.7)	21.9 ± 28.3 (6.2–85.7)	0.81 ± 0.15 (0.67–1.20)
Wirestam et al.[9]	20 ± 9	14 ± 53	N/R
Rydhog et al.[4]: average°	5.3 ± 1.6	86 ± 14	0.83 ± 0.06
Grech-Sollars et al.[35]	10.0	N/R	0.75
Wu et al.[10]	14 ± 2	8.2 ± 0.9	0.84 ± 0.05
Filli et al.[5]	3.48 ± 1.58	12.33 ± 4.06	0.67 ± 0.05
Federau et al.[6^]	4.7 ± 3.0	17.0 ± 11.3	0.72 ± 0.05
Ahlgren et al.[7°]	2.4 ± 0.8	N/R	1.20 ± 0.22
Stieb et al.[11+]	12.5	9.95	0.75
Wang et al.[25]: average	24.7	N/R	0.72
Wong et al.[26]	2.40 ± 0.04	N/R	0.73 ± 0.03
Finkenstaedt et al.[36a]	10 ± 3	6.22 ± 0.48	0.91 ± 0.09
White matter			
Average over published values*	6.8 ± 4.9 (1.6–16.0)	25.3 ± 29.1 (7.9–84.0)	0.74 ± 0.12 (0.61–0.98)
Wirestam et al.[9]	16 ± 8.7	21 ± 60	N/R
Rydhog et al.[4]: average°	3.0 ± 0.3	84 ± 11	0.84 ± 0.03
Grech-Sollars et al.[35]	8.0	N/R	0.65
Filli et al.[5]	3.25 ± 0.94	14.27 ± 3.64	0.64 ± 0.05
Wu et al.[10]	7 ± 1	7.9 ± 0.9	0.77 ± 0.04
Federau et al.[6^]	4.5 ± 1.6	15.1 ± 20.8	0.71 ± 0.05
Ahlgren et al.[7°]	1.6 ± 0.7	N/R	0.98 ± 0.13
Stieb et al.[11+]	9.0	9.79	0.71
Wang et al.[25]: average	13.2	N/R	0.61
Wong et al.[26]	2.21 ± 0.03	N/R	0.72 ± 0.05
Finkenstaedt et al.[36a]	N/R	N/R	N/R

N/R: not reported. *Presented as mean ± standard deviation (range). ^Baseline, non-visual brain. +Fixed-threshold, average over both trials shown. °Considering cortical gray matter. [a]Considering trace values.

using a low number of *b*-values tended to underestimate D^*. There is no clear definition within the literature of how many and which *b*-values to use; for example, Table 2 illustrates the different protocols used in brain IVIM studies. Besides addressing how many *b*-values to use, many studies have attempted to optimize the *b*-value sampling distribution to minimize fit errors. These studies focused on kidney and renal lesions[14] or, with a broader scheme used in simulations, the optimized acquisition schemes were tested in abdominal studies.[15] However, these schemes were based on simulations and used different assumptions that may not always be fulfilled, such as Gaussian noise modelling with no physiological noise or the assumption of fixed specific values for the organ of interest. To the best of the authors' knowledge, no optimized *b*-sampling strategy has been applied to *in vivo* data in the brain, and the question of how to acquire IVIM data in the brain to minimize variability remains open. This study aimed to show that an optimized *b*-value sampling distribution improves IVIM estimation in the brain by decreasing the variance associated with IVIM parameters with respect to regular distribution in healthy volunteers.

Materials and Methods

This study was approved by the Institutional Ethics Committee. A total of 10 healthy subjects (seven males, three females; 24.7 ± 6.8 years old; range: 18–40 years) gave written informed consent to participate in this study. Images were acquired on a 1.5T Philips Achieva Scanner (Philips Healthcare, Best, the Netherlands) using an eight-element head coil. 3D T_1-weighted images were acquired to serve as an anatomical reference to facilitate the positioning of a ROI with a TR/TE of 8/3.7 ms, a flip angle of 8° and a spatial resolution of 1 × 1 × 1 mm^3.

Diffusion images were acquired using conventional pulsed gradient spin echo echo planar imaging (EPI) by considering 22 slices with a slice thickness of 5 mm and a gap of 1 mm, a FOV of 230 mm, a matrix of 128 × 128, a TR/TE of 4000/110 ms and an acceleration factor of 2, using sensitivity encoding (SENSE) algorithm. Diffusion weighting was applied along three perpendicular directions. The SNR in non-DWIs (b_0 map), evaluated in different ROI located in white matter, was 151:1 ± 20:1. In DWIs with the highest *b*-values, the SNR was 74:1 ± 11:1.

Two main points were considered when choosing the number of *b*-values to use: first, a compromise was considered to maintain the total acquisition time within what was judged by the authors to be clinically acceptable for the patient and for the total exam time of a full brain protocol, below 5 min. Second, a slight trend toward using 16 values was considered, as observed in 4 of the 11 *b*-value sampling strategies shown in Table 2, agreeing with the conclusion of ter Voert et al.[21] who recommended a minimum of 16 *b*-values in their application. This is also in agreement with the upper limit of *b*-value numbers in some scanners for their conventional diffusion sequences. A maximum *b*-value of 1000 s/mm^2 was chosen as it is a widely-used diffusion weighting for clinical brain studies.[23]

Two distributions of *b*-values were proposed, both of which included 16 values. The acquisition time was kept constant (3 min 12 s) for each set, and the same amount of data points were obtained in each case. The first distribution aimed to sample data in an optimal way. The sampling scheme was based on the one proposed by Lemke et al.[15] The set of *b*-values was obtained using Monte-Carlo simulation, using error of the fit as optimization criterion, starting from three *b*-values of [0, 40, 1000] s/mm^2, including more *b*-values in the range of [0, 1000] in steps of 10 s/mm^2. They considered low diffusion regime for the brain, assuming in this simulation values for *f* of 5%, *D* of 1 × 10^{-3} mm^2/s, and D^* of 10 × 10^{-3} mm^2/s. We used the following set of *b*-values,

Table 2 *b*-Values used in IVIM studies undertaken in the brain of healthy volunteers reported in Table 1

	Number of *b*-values	*b*-Values used (s/mm^2)
Grech-Sollars et al.[35]	7	0, 50, 100, 300, 500, 600, 1000
Filli et al.[5]	8	0, 10, 20, 50, 150, 300, 500, 800
Stieb et al.[11]	9	0, 10, 20, 40, 80, 160, 320, 640, 1280
Wu et al.[10]	12	0, 15, 30, 45, 60, 100, 250, 400, 550, 700, 850, 1000
Wang et al.[25]	14	0, 10, 20, 40, 60, 100, 140, 160, 200, 300, 500, 1000, 1500, 2000
Wong et al.[26]	15	0, 5, 7, 10, 15, 20, 30, 40, 50, 60, 100, 200, 400, 700, 1000
Federau et al.[6]	16	0, 10, 20, 40, 80, 110, 140, 170, 200, 300, 400, 500, 600, 700, 800, 900
Ahlgren et al.[7]	16	0, 10, 20, 30, 40, 50, 60, 70, 80, 90, 100, 120, 140, 180, 200
Finkenstaedt et al.[36]	22	0, 5, 10, 20, 35, 55, 80, 110, 150, 200, 300, 500, 750, 1000, 1300, 110, 150, 200, 300, 500, 750, 1000
Wirestam et al.[9]	36	0, 10, 20, … 100, 120, 140, …, 200, 250, 300, … 1200
Rydhog et al.[4]	64	0–900 s/mm^2, with a higher density of *b*-values in the lower end of this range

IVIM, intravoxel incoherent motion.

[15, 60, 150, 160, 170, 190, 200, 260, 440, 560, 600, 700, 980, 1000] s/mm^2; this distribution was referred to as the 'optimized' distribution throughout the rest of the paper. The other sampling scheme was chosen to provide a choice of *b*-values with a stronger emphasis on low *b*-values, identical to the distribution referred to in the work by Lemke et al.,[15] and Luciani et al.[24] and close to distributions found in the literature.[10,25,26] The values used were [24, 30, 40, 50, 60, 70, 80, 90, 100, 150, 200, 400, 800, 1000] s/mm^2; this distribution is referred to as the 'regular' distribution.

Images were processed using an in-house code developed in MATLAB (MathWorks, Natick, MA, USA). The perfusion f, D^* and D were adjusted according to Eq. [1]. IVIM parameters were fitted in two steps as this was the method of choice of Meeus et al.,[27] and Park et al.[28] in low perfused tissues, in agreement with the conclusion of other groups.[28,29] First, D was adjusted considering only data from *b*-values >200 s/mm^2. Second, D^* and f were adjusted using data from all *b*-values. Fit was done using the trust region reflective algorithm.[30] The quality of fit was registered through the squared norm of the residuals. Processing was performed on DWIs averaged over the three diffusion directions.

To compare the results from each acquisition, results in ROI were contrasted on a one-to-one basis. To minimize the dependence on the user definition of ROI, an automated process was used. In the GM, analysis was based on the 120 ROI defined in the Automated Anatomical Labeling (AAL) atlas.[31] To do this, the AAL template was registered onto DWIs using SPM12,[32] non-normalized mutual information and nearest-neighbor approximation.[33] The quality of registration was confirmed visually and was not accepted in one case (out of the 10 volunteers). In the white matter (WM), a ROI was considered in each hemisphere. T_1-weighted images were first registered onto DWIs in a similar way to that previously described.[33] Images were subsequently segmented using SPM12 and separated according to each hemisphere. As the aim was to compare behavior over the distribution of IVIM parameters within a ROI, a fitting algorithm was run over a series of mini-ROI within each ROI. As many mini-ROI as possible were defined within a ROI, and a mini-ROI was defined as a region of 3 × 3 × 3 pixels in GM and 5 × 5 × 3 pixels in WM. IVIM parameters were fit over the average signal in these mini-ROI. To work on many mini-ROI within one anatomical area permits to run further statistical analysis within that area in comparison to working with the analysis run on a single AAL ROI. Maps were obtained after 2D Gaussian filtering (0.75 standard deviation) of the DWIs.

A comparison of the distribution of IVIM parameters from each ROI was undertaken on a one-to-one basis between 'optimized' and 'regular' *b*-value distributions if the ROI contained a minimum of 20 mini-ROI (Fig. 1). Therefore, considering all the volunteers and defined ROI, the analysis was performed for 832 ROI. The normality of distribution within a ROI was tested using Lilliefors test (α: 5%),[34] and the distribution was non-normal in most cases (~90%). Comparison of mean values was performed using the Wilcoxon signed-rank test, and comparison of dispersion was performed using the Ansari–Bradley test.[36] Coefficients of variation (CV) were calculated for the distribution of parameters obtained from each ROI, with the CV being the ratio of standard deviation over the average value. Comparison of distributions of parameters within each ROI between one acquisition and the other was assessed using the two-sample Kolmogorov–Smirnov test (α: 5%), and comparison of distribution tail was undertaken using one-sided hypothesis test of the same two-sample Kolmogorov–Smirnov test (α: 5%).[34]

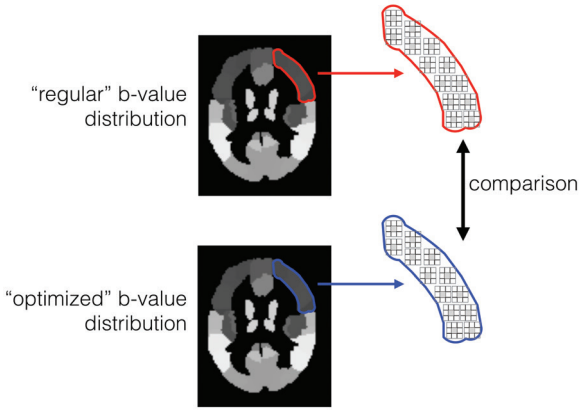

Fig. 1 Graphical representation of the analysis. For each type of acquisition (i.e. using 'regular' or 'optimized' *b*-value distributions), ROI were defined automatically using the Automated Anatomical Labeling (AAL) template. For each ROI, intravoxel incoherent motion (IVIM) parameters were fitted in as many mini-ROI as possible. A comparison of IVIM parameter distributions from each ROI was undertaken.

Results

Example maps of IVIM parameters obtained from each sampling scheme are shown in Fig. 2. Visually, the maps obtained with the 'regular' distribution of *b*-values present more "outlier-like" pixels, in particular in the D^* map. D maps present a very similar appearance in both cases. These differences are confirmed by looking at the distribution of parameters in each ROI analyzed, where an example is shown in Fig. 3: there are dissimilarities in the distribution of parameters fitted from each set of data, more visible in the case of D^* and f. In a majority of cases, distributions are different for f and D^*, mainly due to a heavier tail on the right for the parameter distribution obtained from the 'regular' *b*-value acquisition scheme as detailed in Table 3. The robustness of results obtained from the 'optimized' distribution is also visible through its significantly smaller CV within each ROI for the f and D^* parameters, with a decrease in CV up to 39% in the case of D^*, as detailed in Table 4.

From a quantitative point of view: values averaged over brain areas are given in Table 5: the range of values obtained

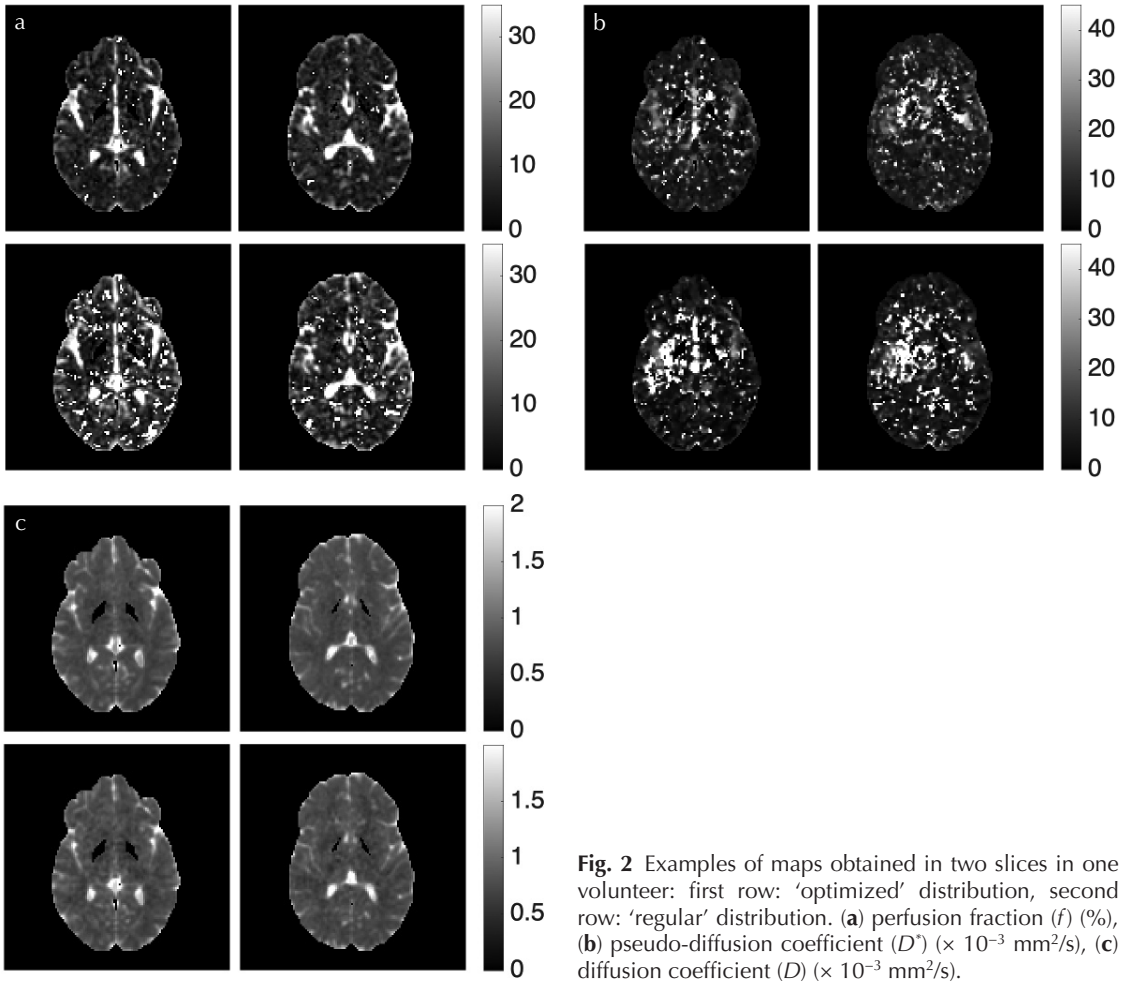

Fig. 2 Examples of maps obtained in two slices in one volunteer: first row: 'optimized' distribution, second row: 'regular' distribution. (**a**) perfusion fraction (f) (%), (**b**) pseudo-diffusion coefficient (D^*) ($\times 10^{-3}$ mm^2/s), (**c**) diffusion coefficient (D) ($\times 10^{-3}$ mm^2/s).

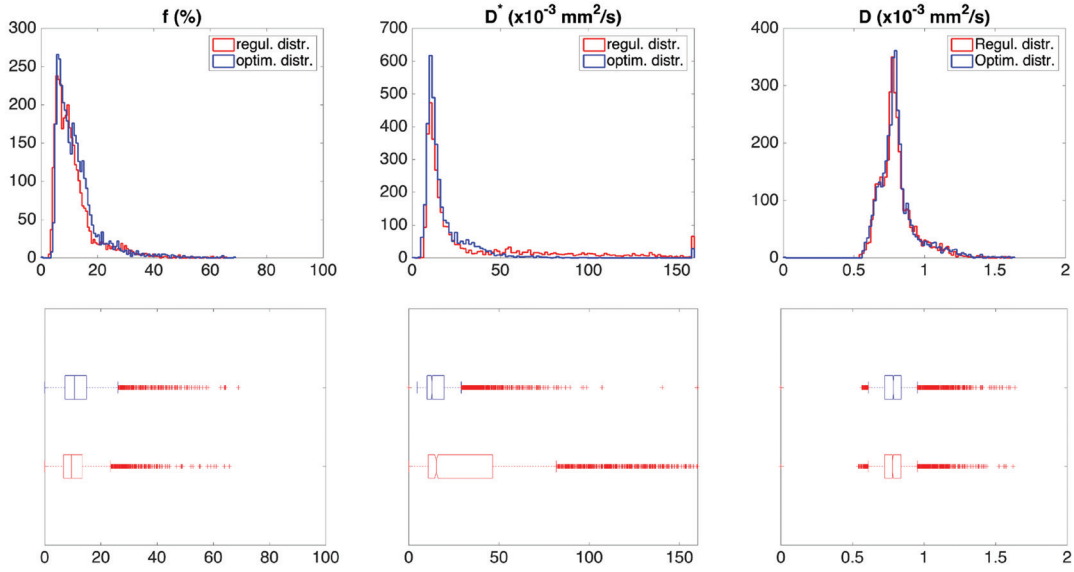

Fig. 3 Examples of histograms (top row) and box plots (bottom row) of parameters estimated with 'regular' distribution (red lines) and 'optimized' distribution (blue lines) within a ROI of one volunteer, of perfusion fraction (left column), pseudo-diffusion coefficient (middle column) and diffusion coefficient (right column). For each row, the x-axis represents the parameter value in units of %, 10^{-3} mm^2/s, and 10^{-3} mm^2/s for the f, D^* and D parameters respectively. For all columns on the top row, the y-axis represents the number of times each value is found. f, fraction; D^*, pseudo-diffusion coefficient; D, diffusion coefficient.

Table 3 Results of distributions comparison over all ROI using Kolmogorov–Smirnov test (N = 832)

	f (%)	D^* (%)	D (%)
Proportion of distributions significantly different between 'regular' and 'optimized' acquisition	50	80	17
Within the distributions that were found different: proportion that show heavier tail on the right for the acquisition with 'regular' b-value distribution	63	74	47

f, fraction; D^*, pseudo-diffusion coefficient; D, diffusion coefficient.

Table 4 Coefficients of variation (CV) values obtained for the analysis within each ROI. The results are presented as mean and standard deviation over all ROI

	f	D^*	D
'Optimized' b-values distribution	0.71 ± 0.36	0.66 ± 0.37	0.20 ± 0.09
'Regular' b-values distribution	0.90 ± 0.42	1.08 ± 0.49	0.20 ± 0.09
P-value	$<10^{-5}$	$<10^{-5}$	0.74
Reduction of CV	21%	39%	–

f, fraction; D^*, pseudo-diffusion coefficient; D, diffusion coefficient.

here agrees with the values published in other studies summarized in Table 1. Considering the gray matter included in regions in the frontal, limbic, occipital, parietal and temporal lobes as well as in the central region and in the subcortical nuclei, the IVIM values observed here with the 'optimized' distribution are in agreement with the ones from the literature: f averages as 13.2 ± 2.8% (median 10.3%) when the average over published values is 10.0 ± 7.4%; D^* averages as 15.89 ± 2.17 × 10^{-3} mm^2/s (median 12.5 × 10^{-3} mm^2/s), when the average over published values is 21.9 ± 28.3 × 10^{-3} mm^2/s. In white matter, f averages as 12.4 ± 2.1% (median 9.6%) when the average over published values is 6.8 ± 4.9%; D^* averages as 14.5 ± 4.2 × 10^{-3} mm^2/s (median 11.6 × 10^{-3} mm^2/s), when the average over published values is 25.3 ± 29.1 × 10^{-3} mm^2/s. When focusing in particular on the perfusion fraction as it shows smaller range of variation over published values than D^*, our results are coherent with the ones from different groups that worked on estimating multi-center reproducibility,[35] robustness of IVIM parameters,[10] test–retest reliability[11] and on exploring the anisotropy associated with microperfusion[36]: the f-values from these groups range from 10 to 14% in case of gray matter, and from 7 to 9% in white matter. Diffusion coefficients values from our observations are in good agreement with literature values: we obtained 0.87 ± 0.04 × 10^{-3} mm^2/s vs. 0.81 ± 0.15 × 10^{-3} mm^2/s in gray matter and 0.91 ± 0.12 × 10^{-3} mm^2/s vs. 0.74 ± 0.12 × 10^{-3} mm^2/s in white matter.

The range of values obtained with the 'regular' distribution is broader than the one obtained with the 'optimized' distribution for both f and D^* parameters. For the perfusion fraction, the observed range is 7.83% in the 'optimized' case and 11.19% in the 'regular' case; and for the pseudo-diffusion coefficient, the observed range is 6.96 × 10^{-3} mm^2/s for the 'optimized' case and 11.78 × 10^{-3} mm^2/s in the 'regular' case. This reflects a tendency for higher dispersion of values in the case of 'regular' b-value distribution, similar to what is seen in distributions of parameters within ROI seen in Fig. 3. The quantification of the CV estimated between cortical areas in Table 5 also shows a bigger variance of results in the case of acquisitions with a 'regular' b-sampling scheme than with an 'optimized' sampling scheme for the pseudo-diffusion coefficient. In the central region, cerebellum, limbic and temporal lobes out of the nine brain areas studied here, D^* values were found significantly different between 'regular' and 'optimized' acquisitions. When there is a significant difference in mean values obtained from each analysis, the difference decreases when considering median values, for instance in the temporal lobe: average D^* values in the 'regular' and 'optimized' distributions are 24.8 ± 8.3 vs. 15.3 ± 3.7 × 10^{-3} mm^2/s respectively, while the median values are 14.1 vs. 11.8 × 10^{-3} mm^2/s respectively, showing considerably smaller difference. This reinforces the fact that the difference observed between the two acquisitions come from the presence of outlier-like values, more frequently encountered in the case of the 'regular' distribution. In these cases, D^* estimated from the 'regular' acquisition has higher values than in the 'optimized' acquisition, meaning that the initial slope of signal decay is overestimated. This occurs more frequently in regions where the initial signal decay is faster such as in areas with more partial volume effect with blood vessels or with cerebrospinal fluid (CSF). This effect is illustrated in Fig. 4, where DWIs from the first five b-values in each acquisition show signal differences in the Sylvian cistern (temporal lobe). There are no differences in the f and D maps obtained from the 'regular' and 'optimized' distribution, but the D^* maps obtained from each distribution are different particularly close to the Sylvian cistern. This is probably the reason why the quantitative analysis shown in Table 5 presents significant differences in brain areas that are more prone to this kind of effect.

Discussion

The purpose of this study was to emphasize the importance of the sampling scheme used to estimate IVIM parameters. From a quantitative point of view, the lack of a gold standard and the broad range of values published make strict comparisons difficult; nevertheless, the range of values obtained here is in agreement with the ones published in the literature, as summarized in Tables 1 and 5. We used here a scheme based on the optimization done by Lemke et al.[15] in contrast with another sampling scheme considered as 'regular' in contrast to the 'optimized' scheme. Resulting maps of IVIM parameters are qualitatively different with more "speckles" in the f and D^* maps obtained from 'regular' distribution, similarly as Lemke

Table 5

	'Optimized' distribution		'Regular' distribution	
	Mean ± std. dev.	Median	Mean ± std. dev.	Median
f (%)				
Central region	13.31 ± 2.75	11.26	12.54 ± 1.79	10.41
Cerebellum	13.85 ± 1.82	10.72	14.72 ± 2.20	10.47
Frontal lobe	11.69 ± 2.52	9.53	11.52 ± 2.47	8.92
Limbic lobe	11.95 ± 2.93	10.02	22.39 ± 7.37	16.42
Occipital lobe	17.60 ± 3.65	12.38	19.70 ± 6.20	13.01
Parietal lobe	16.36 ± 6.58	11.25	18.79 ± 6.96	11.72
Subcortical nuclei	9.77 ± 1.97	7.59	11.20 ± 2.85	7.94
Temporal lobe	11.80 ± 3.94	9.95	11.40 ± 2.85	9.00
White matter	12.38 ± 2.07	9.61	13.65 ± 2.44	9.27
Average ± std. dev. (range)	13.19 ± 2.45 (9.77–17.60)	10.26 ± 1.37 (7.59–12.38)	15.10 ± 4.16 (11.20–22.39)	10.80 ± 2.62 (7.94–16.42)
Average CV	0.23 ± 0.08		0.25 ± 0.08	
D^* ($\times 10^{-3}$ mm^2/s)				
Central region	15.64 ± 2.17	13.45	24.69 ± 7.39**	16.98
Cerebellum	14.25 ± 2.99	10.67	19.73 ± 5.88**	11.92
Frontal lobe	12.64 ± 2.76	10.84	18.53 ± 6.63	12.54
Limbic lobe	15.29 ± 2.32	12.38	30.31 ± 11.15**	16.18
Occipital lobe	19.60 ± 14.61	14.24	19.89 ± 11.12	10.45
Parietal lobe	17.55 ± 9.14	14.24	28.59 ± 21.12	20.01
Subcortical nuclei	15.26 ± 5.02	10.86	19.55 ± 8.16	11.37
Temporal lobe	15.27 ± 3.65	11.75	24.76 ± 8.32**	14.05
White matter	14.54 ± 4.24	11.59	20.44 ± 8.65	12.99
Average ± std. dev. (range)	15.56 ± 1.99 (12.64–19.60)	12.24 ± 1.46 (10.67–14.37)	22.94 ± 4.32 (18.53–30.31)	14.05 ± 3.10 (10.45–20.01)
Average CV	0.32 ± 0.20		0.42 ± 0.14	
D ($\times 10^{-3}$ mm^2/s)				
Central region	0.92 ± 0.11	0.88	0.91 ± 0.10	0.88
Cerebellum	0.93 ± 0.13	0.89	0.92 ± 0.13	0.88
Frontal lobe	0.90 ± 0.09	0.86	0.90 ± 0.08	0.85
Limbic lobe	0.87 ± 0.10	0.84	0.87 ± 0.09	0.84
Occipital lobe	0.89 ± 0.13	0.86	0.91 ± 0.12	0.86
Parietal lobe	0.80 ± 0.12	0.78	0.81 ± 0.10	0.79
Subcortical nuclei	0.86 ± 0.09	0.83	0.86 ± 0.09	0.83
Temporal lobe	0.87 ± 0.11	0.84	0.88 ± 0.10	0.84
White matter	0.91 ± 0.12	0.87	0.91 ± 0.12	0.86
Average ± std. dev. (range)	0.89 ± 0.04 (0.80–0.93)	0.85 ± 0.03 (0.78–0.89)	0.88 ± 0.04 (0.81–0.92)	0.85 ± 0.03 (0.79–0.88)
Average CV	0.13 ± 0.02		0.12 ± 0.02	

f, D^* and *D* values obtained using the 'regular' and the 'optimized' *b*-value distribution using the two-steps fit method. Data are presented as mean and standard deviation for the ROIs identified within certain grey matter (GM) areas defined according to the AAL atlas[30] or in white matter. Specifically: the "Central Region" is composed of GM in the precentral gyrus, postcentral gyrus, and Rolandic operculum. The "Frontal Lobe" region is composed of GM, in its lateral surface: superior frontal gyrus - dorsolateral, middle frontal gyrus, inferior frontal gyrus with opercular and triangular parts; in its medial surface: superior frontal gyrus-medial, supplementary motor area, paracentral lobule; in its orbital surface: superior frontal gyrus, orbital and medial orbital parts, middle and inferior frontal gyrus — orbital parts, gyrus rectus, olfactory cortex. The "Limbic Lobe" region is composed of GM in the temporal pole: superior temporal gyrus and middle temporal gyrus, anterior cingulate and paracingulate gyri, middle cingulate and paracingulate gyri, posterior cingulate gyrus; hippocampus, parahippocampal gyrus, insula. The "Occipital Lobe" region is composed of GM in its lateral surface: superior, middle and inferior occipital gyri; in its medial and inferior surfaces: cuneus, calcarine fissure, and surrounding cortex, lingual gyrus and fusiform gyrus. The "Parietal Lobe" region is composed of GM in its lateral surface: superior parietal gyrus, inferior parietal gyrus; in its medial surface: precuneus. The "subcortical nuclei" region is composed of amygdala, caudate nucleus, putamen, pallidum, thalamus. The "Temporal Lobe" region is composed of GM in its lateral surface: superior temporal gyrus, Heschl's gyrus, middle and inferior temporal gyri.**Indicates significance difference between optimized and regular distribution (α: 1%). *f*, fraction; D^*, pseudo-diffusion coefficient; *D*, diffusion coefficient; std. dev., standard deviation; CV, coefficients of variation.

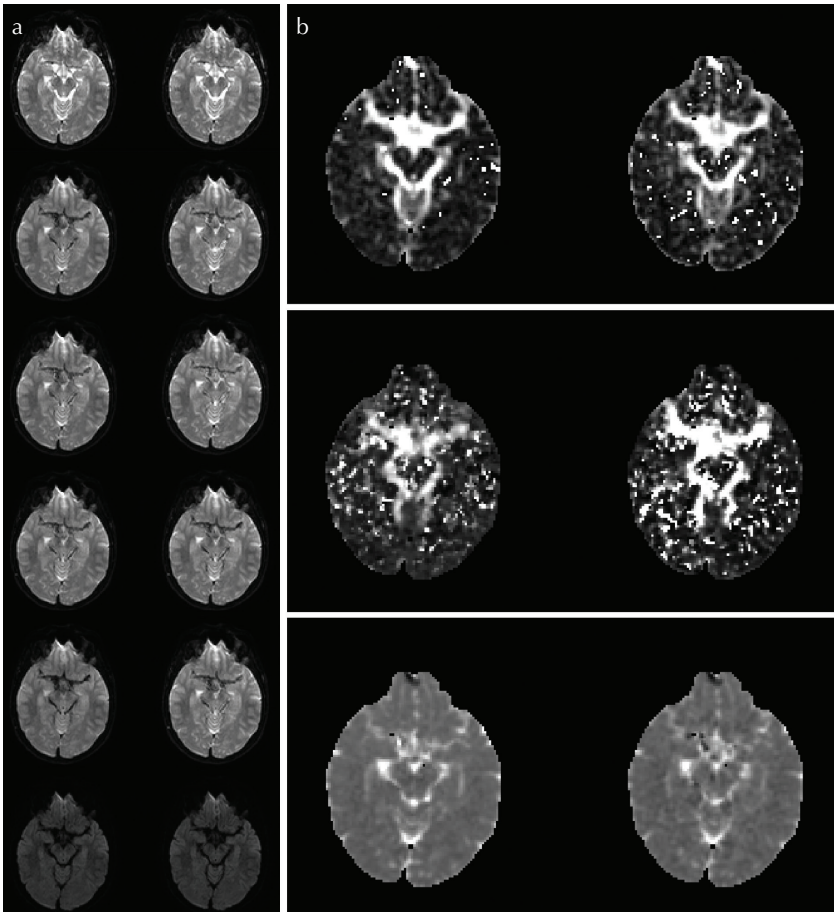

Fig. 4 (**a**) Left column: example of the first five diffusion-weighted images obtained with the 'optimized' distribution with, from top to bottom, b = 0, 40, 50, 60, 150 and 1000 s/mm^2. Right column: example of the first five diffusion-weighted images obtained with the 'regular' distribution with, from top to bottom, b = 0, 10, 20, 30, 40 and 1000 s/mm^2. (**b**) Left column: maps obtained with the 'optimized' distribution. Right column: maps obtained with the 'regular' distribution. Top row: Perfusion fraction (f) maps. Middle row: diffusion coefficient (D) maps. Bottom row: D maps. Note the difference in the pseudo-diffusion coefficient (D^*) maps around the Sylvian cistern.

et al.[15] observed in abdominal images. Significant differences are observed in f and D^* distributions obtained in a majority of ROI defined using an automatic procedure. Less variability is obtained when the sampling scheme is optimized, as quantified through smaller CV. This translates into a less broad range of values of f and D^* obtained over cortical areas, summarized in Table 5. The most sensitive parameter to this is the pseudo-diffusion coefficient D^*. Our interpretation is that, by using an optimized b-value sampling scheme, data are obtained in a way that allows a better characterization of the signal decay: data are sampled in better adequacy for the fitting of a bi-exponential model. Consequently, when an adjustment of the curve is made by using a regular sampling scheme, this scheme may not be considering the critical points of the curvature of the function which would cause a modeling error. This modeling error would have a direct effect on the statistical estimation procedure, resulting in a model that does not adequately explain the mapping of the data and that is reflected mainly in an increase of residuals errors and a more significant presence of outliers. On the other hand, when an optimized sampling scheme is available, the characteristics of the curve are better represented, so that better goodness of fit of the regression curve is obtained.

It is important to stress that both acquisitions to obtain IVIM parameters maps are similar in the sense of presenting the same SNR, and the same quantity of data points (same amount of b-values) to adjust the same bi-exponential model with the same algorithm. Our interpretation of the different results comes from the fact that the sampling scheme used in one case is better adapted to the problem than the other sampling scheme. Figure 5 exemplifies how different sampling gives different data and different results for the fitted parameters. This translates into the visualizations presented in Fig. 4: the description of the initial signal decay is not obtained the same way according to which b-value sampling scheme is used, and the fitting of the initial slope, D^*, is more sensitive to partial volume effects or other kinds of artifacts.

It has been reported that it is important to have sufficiently high SNR to obtain reliable IVIM estimation.[4,15,27] According to Lemke et al.,[15] a critical value for the SNR is 50:1. SNR in our T_2-weighted images is around 150:1 and around 75:1 in the DWI with higher b-values: SNR in our images are higher than critical values. Besides, we also included spatial averaging of the data, which will decrease the impact of noise on the estimation.

One of the limitations of this study is that the effects of different tissues or CSF relaxation effects are not accounted for, while Bisdas et al.[37] showed an impact on the perfusion fraction parameter at varying echo time.[37] As acquisitions

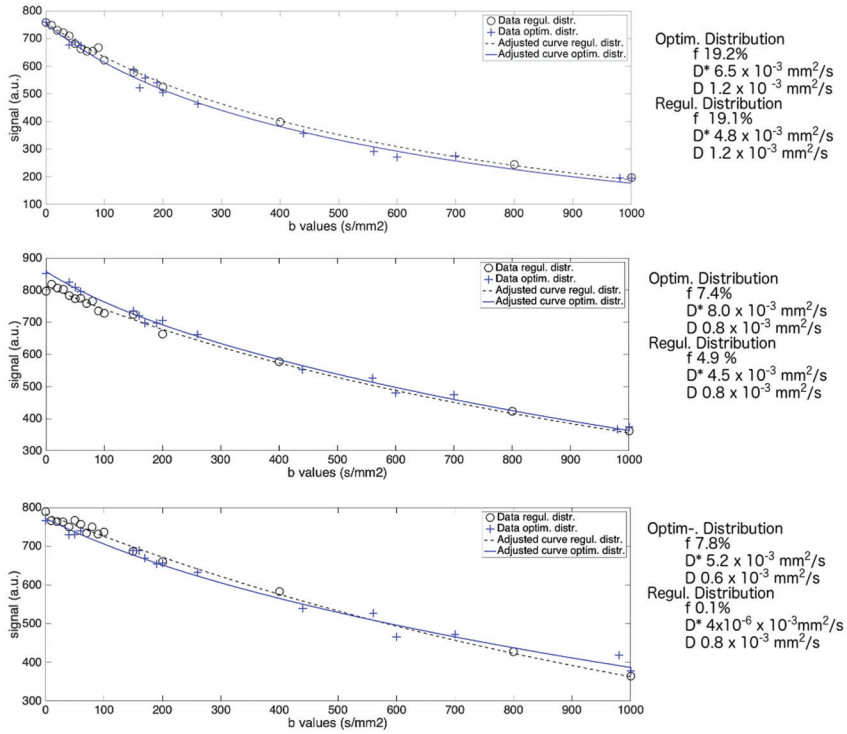

Fig. 5 Examples of data obtained in three different pixels using 'optimized' and 'regular' distribution. Top row: *f* and *D* obtained with both distributions are very close but D^* differ. Middle row: *D* obtained with both distributions are similar but *f* and D^* differ. Bottom row: mainly one component is detected in the 'regular' distribution data, with D^* being very close to 0. *f*, fraction; D^*, pseudo-diffusion coefficient; *D*, diffusion coefficient.

were done maintaining all parameters equal, TE equal, but sampling scheme in both cases, potential contamination of different tissues would be present in a similar manner in both cases and the conclusion obtained should not change. To minimize the effect of CSF contamination in IVIM results, Bisdas et al.[37] chose to mask pixels with relevant CSF partial volume. As the purpose was to show that the choice of *b*-value sampling scheme can have an impact on the robustness of the IVIM parameters estimation, the decision was made not to mask those pixels. Table 5 and Fig. 4 exemplify the better robustness of an 'optimized' *b*-value sampling scheme over a 'regular' one. Besides, the analysis was done in an automatic manner, defining regions of interest according to the proposal by the AAL template: there is no potential bias in an analysis or in the other by a user reading of the images to have included a region with more CSF contamination.

The CV values reported in Table 4 may seem high, however, it is important to underline that variation was quantified in a slightly different way in this study. This study focused on estimating variation for 'mini-ROI' within a ROI, which was defined automatically according to the AAL atlas. The CV usually quantifies an estimation of the variation within a ROI when repeating the measure itself. Quantification of variability between cortical area, in Table 5, shows CV between 0.12 and 0.42. Our understanding is that the relatively high CV values quantified in Table 4 (0.66 or higher), observed in both cases of 'optimized' and 'regular' distributions for the *f* and D^* parameters, are related to the fact that the assumption that the template-defined ROI are homogeneous may be discussed and may generate a higher variability than expected. This is coherent with the observations in Table 5, where a broad range of values across the brain were obtained for *f* and D^*. It is important to stress that, in each case, the analysis was performed without user interaction, using the same definition of ROI and using the same methodology for distribution comparison over the 832 ROI (analyzed one-to-one), thus giving confidence in the observation of decreased variability.

The anatomical regions listed in Table 5 present different values for *f* and D^* parameters among anatomical regions, leading to the question of whether regional differences in micro-perfusion could be evaluated with IVIM. Previous works have reported differences in perfusion between anatomical structures in MRI using arterial spin labeling techniques,[38,39] in particular some areas have been shown to have higher cerebral blood flow such as the Heschl gyrus (in temporal lobe), cingulate (in limbic lobe), thalamus (in subcortical nuclei). What is established is the dependence of perfusion on age,[38,39] a factor that has not been taken into account here. Few works have explored the anatomical dependency of IVIM parameters within brain structures.[3,40] Increased precision for IVIM estimation, which is what is aimed in this study, is needed to allow deepening the exploration of variability between anatomical structure.

Part of the difficulty of working with IVIM acquisition is that there is no gold standard value to confirm which values are to be expected in healthy tissues. Our results show here improved precision when using an 'optimized' *b*-value distribution, which does not mean improved accuracy. Lemke et al.[15] also reported an effect on the estimation variance at

using different *b*-value distributions, based on simulation and observation on abdominal images in three volunteers. The observations reported here are based on the study of nine volunteers who were assessed on one site using one 'optimized' distribution versus one 'regular' distribution, with observations made using a systematic comparison that was not user dependent. The point to be emphasized is that higher precision of IVIM parameters can be attained when acquiring images using an optimized *b*-value distribution, as was observed here for low-perfused tissues such as those in the brain. For the IVIM observations to give clear information to support diagnostic, it is relevant to decrease as much as possible the variability due to the method used. What is stressed in this work is that one of the sources of variability is the *b*-value sampling scheme. It has been shown by other groups that the IVIM results may depend on the fitting methods.[27–29,41,42] Further work is needed to study the impact of the sampling scheme in combination with these other sources of variability that have been observed.

Conclusion

This work shows that an optimized *b*-value sampling scheme improves the estimation of IVIM parameters in a low-perfused organ by decreasing the associated variance in comparison with 'regular' *b*-value sampling scheme; a smaller range of values is observed in the adjusted parameters. This effect is visible qualitatively on the images as f and D^* maps with fewer speckles are obtained. Our interpretation is that, while data are sampled in a more adequate way, a better description of the signal decay is obtained and precision is gained in the estimation of a bi-exponential model.

In this work, it is important to highlight that a researcher independent computational framework has been proposed for the validation process of the impact of the *b*-values sampling schemes on the brain IVIM estimation. This scheme prevents the researcher from introducing biases in the validation process since it does not involve the researcher's interaction. This scheme could be extended to other experimental studies where it is required to analyze the influence effect of some factor or co-factor, either in the modeling or in its adjustment.

Additional work remains to be done to extend this conclusion to different field strengths, different sites and different methods of adjustment. The interest of using an optimized *b*-value sampling scheme is to gain precision; this would be of help to detect small variations in IVIM parameters in healthy subjects and different pathological conditions, as interest was shown in using f and D^* as potential biomarkers in gliomas and glioblastomas.[43,44]

Funding

This work was supported by a CONICYT–PIA–Anillo grant [ACT1416; PMI UVA 1402]. SU, SC acknowledge funding support from Millenium Science Initiative of the Ministry of Economy, Development and Tourism, grant Nucleus for Cardiovascular Magnetic Resonance.

Conflicts of Interest

The authors declare that they have no conflicts of interest.

References

1. Le Bihan D, Breton E, Lallemand D, Aubin ML, Vignaud J, Laval-Jeantet M. Separation of diffusion and perfusion in intravoxel incoherent motion MR imaging. Radiology 1988; 168:497–505.
2. Iima M, Le Bihan D. Clinical intravoxel incoherent motion and diffusion MR imaging: past, present, and future. Radiology 2016; 278:13–32.
3. Federau C. Intravoxel incoherent motion MRI as a means to measure *in vivo* perfusion: a review of the evidence. NMR Biomed 2017; 30:e3650. doi: 10.1002/nbm.3793.
4. Rydhög AS, van Osch MJ, Lindgren E, et al. Intravoxel incoherent motion (IVIM) imaging at different magnetic field strengths: what is feasible? Magn Reson Imaging 2014; 32:1247–1258.
5. Filli L, Wurnig MC, Luechinger R, Eberhardt C, Guggenberger R, Boss A. Whole-body intravoxel incoherent motion imaging. Eur Radiol 2015; 25:2049–2058.
6. Federau C, O'Brien K, Birbaumer A, Meuli R, Hagmann P, Maeder P. Functional mapping of the human visual cortex with intravoxel incoherent motion MRI. PLoS One 2015; 10:e0117706. doi: 10.1371/journal.pone.0117706
7. Ahlgren A, Knutsson L, Wirestam R, et al. Quantification of microcirculatory parameters by joint analysis of flow-compensated and non-flow-compensated intravoxel incoherent motion (IVIM) data. NMR Biomed 2016; 29:640–649.
8. Zhang X, Ingo C, Teeuwisse WM, Chen Z, van Osch MJP. Comparison of perfusion signal acquired by arterial spin labeling-prepared intravoxel incoherent motion (IVIM) MRI and conventional IVIM MRI to unravel the origin of the IVIM signal. Magn Reson Med 2018; 79:723–729.
9. Wirestam R, Borg M, Brockstedt S, Lindgren A, Holtås S, Ståhlberg F. Perfusion-related parameters in intravoxel incoherent motion MR imaging compared with CBV and CBF measured by dynamic susceptibility-contrast MR technique. Acta Radiol 2001; 42:123–128.
10. Wu WC, Chen YF, Tseng HM, Yang SC, My PC. Caveat of measuring perfusion indexes using intravoxel incoherent motion magnetic resonance imaging in the human brain. Eur Radiol 2015; 25:2485–2492.
11. Stieb S, Boss A, Wurnig MC, et al. Non-parametric intravoxel incoherent motion analysis in patients with intracranial lesions: test–retest reliability and correlation with arterial spin labeling. Neuroimage Clin 2016; 11:780–788.
12. Rydhög AS, Szczepankiewicz F, Wirestam R, et al. Separating blood and water: perfusion and free water elimination from diffusion MRI in the human brain. Neuroimage 2017; 156:423–434.

13. Yao Y, Zhang S, Tang X, et al. Intravoxel incoherent motion diffusion-weighted imaging in stroke patients: initial clinical experience. Clin Radiol 2016; 71:938.e11–938.e16.
14. Zhang JL, Sigmund EE, Rusinek H, et al. Optimization of *b*-value sampling for diffusion-weighted imaging of the kidney. Magn Reson Med 2012; 67:89–97.
15. Lemke A, Stieltjes B, Schad LR, Laun FB. Toward an optimal distribution of *b* values for intravoxel incoherent motion imaging. Magn Reson Imaging 2011; 29:766–776.
16. Cho GY, Moy L, Zhang JL, et al. Comparison of fitting methods and *b*-value sampling strategies for intravoxel incoherent motion in breast cancer. Magn Reson Med 2015; 74:1077–1085.
17. Dyvorne H, Jajamovich G, Kakite S, Kuehn B, Taouli B. Intravoxel incoherent motion diffusion imaging of the liver: optimal *b*-value subsampling and impact on parameter precision and reproducibility. Eur J Radiol 2014; 83:2109–2113.
18. Jambor I, Merisaari H, Aronen HJ, et al. Optimization of *b*-value distribution for biexponential diffusion-weighted MR imaging of normal prostate. J Magn Reson Imaging 2014; 39:1213–1222.
19. Conklin J, Heyn C, Roux M, Cerny M, Wintermark M, Federau C. A simplified model for intravoxel incoherent motion perfusion imaging of the brain. AJNR Am J Neuroradiol 2016; 37:2251–2257.
20. Meeus EM, Novak J, Dehghani H, Peet AC. Rapid measurement of intravoxel incoherent motion (IVIM) derived perfusion fraction for clinical magnetic resonance imaging. MAGMA 2018; 31:269–283.
21. ter Voert EE, Delso G, Porto M, Huellner M, Veit-Haibach P. Intravoxel incoherent motion protocol evaluation and data quality in normal and malignant liver tissue and comparison to the literature. Invest Radiol 2016; 51: 90–99.
22. Cohen AD, Schieke MC, Hohenwalter MD, Schmainda KM. The effect of low *b*-values on the intravoxel incoherent motion derived pseudodiffusion parameter in liver. Magn Reson Med 2015; 73:306–311.
23. Korfiatis P, Erickson B. The basics of diffusion and perfusion imaging in brain tumors. Appl Radiol 2014; 43:22–29.
24. Luciani A, Vignaud A, Cavet M, et al. Liver cirrhosis: intravoxel incoherent motion MR imaging—pilot study. Radiology 2008; 249:891–899.
25. Wang C, Ren D, Guo Y, et al. Distribution of intravoxel incoherent motion MRI-related parameters in the brain: evidence of interhemispheric asymmetry. Clin Radiol 2017; 72:94.e1–94.e6.
26. Wong SM, Zhang CE, van Bussel FC, et al. Simultaneous investigation of microvasculature and parenchyma in cerebral small vessel disease using intravoxel incoherent motion imaging. Neuroimage Clin 2017; 14:216–221.
27. Meeus EM, Novak J, Withey SB, Zarinabad N, Dehghani H, Peet AC. Evaluation of intravoxel incoherent motion fitting methods in low-perfused tissue. J Magn Reson Imaging 2017; 45:1325–1334.
28. Park HJ, Sung YS, Lee SS, et al. Intravoxel incoherent motion diffusion-weighted MRI of the abdomen: the effect of fitting algorithms on the accuracy and reliability of the parameters. J Magn Reson Imaging 2017; 45:1637–1647.
29. Suo S, Lin N, Wang H, et al. Intravoxel incoherent motion diffusion-weighted MR imaging of breast cancer at 3.0 tesla: comparison of different curve-fitting methods. J Magn Reson Imaging 2015; 42:362–370.
30. Byrd RH, Schnabel RB, Shultz GA. Approximate solution of the trust region problem by minimization over two-dimensional subspaces. Math Program 1988; 40:247–263.
31. Rolls ET, Joliot M, Tzourio-Mazoyer N. Implementation of a new parcellation of the orbitofrontal cortex in the automated anatomical labeling atlas. Neuroimage 2015; 122:1–5.
32. Statistical Parametric Mapping. http://www.fil.ion.ucl.ac.uk/spm/. (Accessed June 14, 2018).
33. Collignon A, Maes F, Delaere D, Vandermeulen D, Suetens P, Marchal G. Automated multi-modality image registration based on information theory, In: Bizais Y, Barillot C, Di Paola R, eds. Information Processing in Medical Imaging. Dordrecht, The Netherlands: Kluwer Academic Publishers, 1995; 263–274.
34. Upton G, Cook I. A dictionary of Statistics. 2nd ed. Oxford: Oxford University Press; 2008.
35. Grech-Sollars M, Hales PW, Miyazaki K, et al. Multi-centre reproducibility of diffusion MRI parameters for clinical sequences in the brain. NMR Biomed 2015; 28:468–485.
36. Finkenstaedt T, Klarhoefer M, Eberhardt C, et al. The IVIM signal in the healthy cerebral gray matter: a play of spherical and non-spherical components. Neuroimage 2017; 152:340–347.
37. Bisdas S, Klose U. IVIM analysis of brain tumors: an investigation of the relaxation effects of CSF, blood, and tumor tissue on the estimated perfusion fraction. MAGMA 2015; 28:377–383.
38. Hasan KM, Ali H, Shad MU. Atlas-based and DTI-guided quantification of human brain cerebral blood flow: feasibility, quality assurance, spatial heterogeneity and age effects. Magn Reson Imaging 2013; 31:1445–1452.
39. Haller S, Zaharchuk G, Thomas DL, Lovblad KO, Barkhof F, Golay X. Arterial spin labeling perfusion of the brain: emerging clinical applications. Radiology 2016; 281:337–356.
40. Federau C, Maeder P, O'Brien K, Browaeys P, Meuli R, Hagmann P. Quantitative measurement of brain perfusion with intravoxel incoherent motion MR imaging. Radiology 2012; 265:874–881.
41. Ichikawa S, Motosugi U, Hernando D, et al. Histological grading of hepatocellular carcinomas with intravoxel incoherent motion diffusion-weighted imaging: inconsistent results depending on the fitting method. Magn Reson Med Sci 2018; 17:168–173.
42. Gustafsson O, Montelius M, Starck G, Ljungberg M. Impact of prior distributions and central tendency measures on Bayesian intravoxel incoherent motion model fitting. Magn Reson Med 2018; 79:1674–1683.
43. Puig J, Sánchez-González J, Blasco G, et al. Intravoxel incoherent motion metrics as potential biomarkers for survival in glioblastoma. PLoS One 2016; 11:e0158887 doi: 10.1371/journal.pone.0158887.
44. Federau C, Cerny M, Roux M, et al. IVIM perfusion fraction is prognostic for survival in brain glioma. Clin Neuroradiol 2017; 27:485–492.